LA-9162-MS

UC-20d and UC-20f
Issued: April 1982

LA--9162-MS

DE82 014130

Equilibrium Poloidal Field Distributions in Reversed-Field-Pinch Toroidal Discharges

Don A. Baker
Lawry W. Mann
Kurt F. Schoenberg

Los Alamos Los Alamos National Laboratory
Los Alamos, New Mexico 87545

EQUILIBRIUM POLOIDAL FIELD DISTRIBUTIONS IN REVERSED FIELD PINCH TOROIDAL DISCHARGES

by

Don A. Baker, Lawry W. Mann, and Kurt F. Schoenberg

ABSTRACT

A comparison between the analytic formulae of Shafranov for equilibrium in axisymmetric toroidal reversed field pinch (RFP) systems and fully toroidal numerical solutions of the Grad-Shafranov equation is presented as a function of poloidal beta, internal plasma inductance, and aspect ratio. The Shafranov formula for the equilibrium poloidal field distribution is accurate to within 5% for aspect ratios greater than 2, poloidal betas less than 50%, and for plasma current channels that exceed one-third of the minor toroidal radius. The analytic description for the center shift of the innermost flux surface that encloses the plasma current (the Shafranov shift) is accurate to within 15% for aspect ratios greater than 2 and poloidal betas below 50%, provided the shift does not exceed one-tenth of the minor conducting boundary radius. The behavior of the magnetic axis shift as a function of plasma parameters is included. The Shafranov formulae provide a convenient method for describing the equilibrium behavior of an RFP discharge. Examples illustrating the application of the analytic formulae to the Los Alamos ZT-40M RFP experiment are given.

I. INTRODUCTION

The poloidal field system in a toroidal discharge provides two important functions. It induces the toroidal electric field that drives the plasma current over the duration of the discharge, and it provides the magnetic boundary conditions necessary for plasma equilibrium. In typical reversed field pinch (RFP) experiments, the plasma is contained inside a vacuum vessel,

which comprises or is nested within a conducting shell. External to the shell are the poloidal and toroidal field windings.

For time scales less than a characteristic diffusion time ($\tau \propto \mu\sigma d^2$, where μ, σ, and d are defined as the shell permeability, conductivity, and thickness, respectively), the shell stabilizes the plasma against MHD instabilities and holds the plasma in equilibrium via a distribution of induced current on the inner shell surface. For time scales longer than τ, the plasma equilibrium position will change as the internal field diffuses through the shell. This effect may be partially mitigated by the initial introduction of a vertical magnetic field. However, for time scales comparable to the vertical field diffusion time of the shell, an equilibrium plasma configuration requires a proper time-dependent internal-external field match.

A more severe constraint is imposed by minimizing field errors due to shell gaps and ports. A field mismatch at a gap or port will drive large field perturbations into the plasma column, which can distort equilibrium flux surfaces. The perturbation magnitude, initially determined by the gap or port dimension, grows in time as field diffuses into the gap faces. This effect demonstrates the necessity of proper field matching in the vicinity of a gap or port over the duration of the discharge.

In designing a poloidal field system, an expeditious approach is to use the approximate Shafranov formulae to compute the poloidal field at the shell for a desired plasma equilibrium.[1,2] From this field, the required winding distribution is determined. However, because the Shafranov formulae use expansions in ϵ, the inverse toroidal aspect ratio, questions arise regarding their accuracy as a function of plasma beta, plasma inductance, and toroidal aspect ratio. The purpose of this report is, therefore, to compare the Shafranov formulae with the results of fully toroidal numerical solutions of the Grad-Shafranov equation for a wide range of plasma configurations. In addition, the report addresses the use of external field measurements to deduce plasma properties such as the asymmetry factor Λ and presents specific equilibrium results for the Los Alamos ZT-40M experiment.

II. ANALYTIC FORMULATION

An analytic description of equilibrium field distributions applicable to a wide range of experimental configurations was initially proposed by Shafranov.[1,2] The description employed the macroscopic equations of pressure balance for axisymmetric toroidal systems and resulted in, to first order in ε, the magnetic field distribution at the plasma-vacuum interface required for equilibrium. Although, in general, the equilibrium distribution is a function of internal plasma parameters, the Shafranov results are insensitive to internal plasma structure and hence depend only on the macroscopic characteristics of the plasma column.

For a toroidal plasma discharge of major radius R, with a perfectly conducting shell of minor radius a, and minor plasma radius a′ which denotes the innermost flux surface enclosing the total plasma current (Fig. 1), the equilibrium poloidal field distribution at the shell is given by[1]

$$B_p(a,\theta) = B_o(a)\left[1 + \varepsilon\Lambda^* \operatorname{Cos}(\theta)\right] + O(\varepsilon^2) \quad , \tag{2.1}$$

where

$$\Lambda^* = \frac{\Lambda(a')}{2}\left(1 + \frac{a'^2}{a^2}\right) - \frac{1}{4}\left(1 - \frac{a'^2}{a^2}\right) + \frac{1}{2}\ln\left(\frac{a}{a'}\right) \quad , \tag{2.2}$$

$$\Lambda(a') \equiv \text{the asymmetry factor} = \beta_p(a') + \frac{\ell_1(a')}{2} - 1 \quad , \tag{2.3}$$

$$\beta_p(a') = \frac{2\mu_o[\langle p\rangle - P(a)]}{B_o(a')^2} \quad , \tag{2.4}$$

$$\ell_1(a') = \frac{2\int_o^{a'} B_p^2(r)\, r\, dr}{a'^2 B_o(a')^2} \quad , \text{ and} \tag{2.5}$$

$$B_o(a') = \frac{\mu_o\, \bar{I}_\phi}{2\pi a'} \quad (T) \quad . \tag{2.6}$$

$\langle p \rangle$ denotes plasma pressure averaged over the plasma cross section; P(a) denotes pressure at the vacuum vessel wall; I_ϕ represents the toroidal plasma current; r, the integration variable, is the minor radial coordinate; and ε, the inverse toroidal aspect ratio, is equal to the ratio of minor to major radius of the shell. For $a' = a$, β_p defines the poloidal beta in cylindrical geometry. The dimensionless quantity ℓ_i, defined by Eq. (2.5), is the poloidal inductance per unit length inside the radius a' in electromagnetic units (emu). The corresponding internal inductance in MKS units (L_i) is given by

$$L_i = \frac{\mu_o}{4\pi} \ell_i \ (H/M) \quad . \tag{2.7}$$

To first order in ε, the equilibrium magnetic surfaces have nonconcentric circular cross sections. The center displacement of the plasma surface at radius a' with respect to the geometric minor toroidal axis is given by

$$\Delta_s = \frac{a^2}{2R}\left[\ln\left(\frac{a}{a'}\right) + \left(1 - \frac{a'^2}{a^2}\right)\left(\Lambda(a') + \frac{1}{2}\right)\right] - \frac{aB_v}{B_o(a')} + O(\varepsilon^2) \quad , \tag{2.8}$$

where B_v denotes an externally applied uniform vertical field and $O(\varepsilon^2)$ indicates correction terms of order ε^2. Equation (2.8) is valid for shifts much less than the minor toroidal radius ($\Delta_s << a$). In practice, B_v can be used to fine tune plasma position such that the plasma surface and vacuum chamber are concentric.

Formulae (2.1) and (2.8) are valid for any magnetic flux surface of radius a', which encloses the total toroidal plasma current. For $a = a'$, Eq. (2.1) reduces to

$$B_p(\theta) = B_o(a)\left[1 + \varepsilon\Lambda(a)\ \mathrm{Cos}(\theta)\right] \quad . \tag{2.9}$$

Thus, in the design of a particular experiment, it is only necessary to specify the aspect ratio and range of plasma beta and internal inductance to obtain the toroidal image current distribution in the shell, and thereby estimate the poloidal winding distribution or field control necessary for equilibrium operation. The accuracy of this estimation will be addressed in Section IV.

III. THE EQUILIBRIUM CODE

The Baker-Mann code used to assess the accuracy of the Shafranov formulae was developed in the 1960s to design and study multipole equilibria[3] and adapted to RFP equilibria and stability[4] in the early 1970s. It was also employed for belt pinch[5] and high beta tokamak studies[6] in 1978 and is currently used to support the ZT-40M RFP experiment. The code's long history of successful application to many numerical and analytical problems attests to its accuracy. The equilibrium calculation was run for ideal MHD conditions in toroidal geometry with a diffuse plasma profile.

A. Mathematical Model for the Equilibrium Calculation

The ideal MHD equilibrium equations in rationalized MKS units are given by

$$\vec{j} \times \vec{B} = \nabla p \quad , \tag{3.1}$$

$$\nabla \times \vec{B} = \mu_0 \vec{j} \quad , \text{ and} \tag{3.2}$$

$$\nabla \cdot \vec{B} = 0 \quad , \tag{3.3}$$

where $\vec{j}$ is the plasma current density, $\vec{B}$ the magnetic field, and p denotes the plasma pressure. Using the cylindrical coordinate system shown in Fig. 1, where ρ represents the major radial coordinate and ψ is defined as $(2\pi)^{-1}$ times the poloidal magnetic flux function, Eqs. (3.1) through (3.3) yield the familiar Grad-Shafranov equation:

$$\rho\frac{\partial}{\partial\rho}\left(\frac{1}{\rho}\frac{\partial\psi}{\partial\rho}\right) + \frac{\partial^2\psi}{\partial z^2} + \mu_o\rho^2 p' + ff' = 0 \quad , \tag{3.4}$$

where f is $\mu_o/2\pi$ times the poloidal current flux function and a prime denotes differentiation with respect to ψ. Equation (3.4), together with the specification of the $p(\psi)$ and $f(\psi)$ functions and the value of ψ on the boundary, poses a boundary value problem. For pulsed fields produced inside perfectly conducting walls, the condition that the normal component of B vanish at the wall corresponds to the boundary condition that ψ is a constant. Once ψ is obtained, all other equilibrium quantities of interest are readily computed. In particular, for comparison with Shafranov, the poloidal ($\vec{B}_p$) and toroidal ($\vec{B}_\phi$) fields are computed from the following relationships

$$\vec{B}_p = \frac{1}{\rho}\nabla\psi \times \hat{\phi} = \frac{1}{\rho}\left(-\hat{\rho}\frac{\partial\psi}{\partial z} + \hat{z}\frac{\partial\psi}{\partial\rho}\right) \quad \text{and} \tag{3.5}$$

$$\vec{B}_\phi = (f/\rho)\,\hat{\phi} \quad , \tag{3.6}$$

where $\hat{\phi}$ is the unit vector in the ϕ direction.

Pressure and current profiles are represented by functions that allow shapes characteristic of those observed experimentally and are discussed in the Appendix. Unless otherwise noted, the pressure profiles used in this study were peaked on the magnetic axis and dropped smoothly to zero at the conducting boundary. The maximum pressure value was used to control the poloidal beta. The poloidal current profile was varied in width to change the internal plasma inductance and simulate current pinch effects.

B. Method of Solution

Equation (3.4) is an elliptic differential equation with source terms that can be nonlinear. Because exact analytic solutions are obtainable for only very special (for example, linear) source functions and for simple boundaries, general solutions require numerical techniques. The Baker-Mann code uses the method of successive over-relaxation to solve the finite difference equations on a discrete mesh with rectangular elements. Nonrectangular regions are treated using an algorithm that generates special difference equations at the boundary. A rectangular mesh in (ρ,z) avoids the artificial singularities introduced by the use of toroidal coordinates.

Care must be exercised in the choice of starting values of the ψ function, which is loaded on the finite difference mesh before the relaxation iterations begin. The nonlinearity of the problem leads to nonconvergence for certain choices of starting values. Another complication is that, during the iteration procedure, the magnetic axis shifts for each iteration as the procedure converges on the equilibrium solution. This causes the source term, which is a function of the position of the magnetic axis, to change relative to the finite mesh on each iteration. Despite these complications, this code has obtained solutions for circular, racetrack, D-shaped, and rectangular conducting boundaries for rather crude starting guesses provided one starts at a relatively low beta. The low beta solutions can then be used as an initial guess for high beta solutions.

IV. COMPARISON OF THE ANALYTIC AND NUMERICAL RESULTS

This section defines the validity range of the Shafranov formulae since they use expansions in the inverse aspect ratio ε. For comparison purposes, as is normally done in practice, we will assume that the input quantities ℓ_i and β_p are obtained directly from a cylindrical model without toroidal corrections. However, it is interesting to compare the values of β_p and ℓ_i obtained from the cylindrical model with the toroidally correct values obtained from the Baker-Mann code (Figs. 2 and 3). For toroidal geometry, the generalized definitions of β_p and ℓ_i are given by

$$\beta_p \text{ (toroidal)} = \frac{2\mu_o\langle p\rangle}{\langle B_p(a)\rangle^2} = \frac{8\pi^2 a^2\langle p\rangle}{\mu_o I_\phi^2} \quad , \tag{4.1}$$

where $\langle B_p(a)\rangle$ denotes an average over circumference and $\langle p\rangle$ is computed by averaging over the total toroidal cross section, and

$$\ell_i \text{ (toroidal)} = \frac{2(\text{poloidal field energy})}{2\pi R I_\phi^2} \quad . \tag{4.2}$$

In both cases, the deviation of the cylindrical formulae from their toroidal counterparts is greatest at low aspect ratios and high betas. In addition, the cylindrical formulae always underestimate their corresponding toroidal values.

A. Equilibrium Dependence of the Poloidal Field

Using Eq. (2.9), the ratio of the poloidal field values at the maximum (R_{max}) and minimum (R_{min}) major radial positions on the toroidal midplane is given by

$$\gamma = \frac{B_p(R_{max})}{B_p(R_{min})} = \frac{[1 + \varepsilon\Lambda]}{[1 - \varepsilon\Lambda]} \quad , \tag{4.3}$$

where Λ, the asymmetry factor, is defined by Eq. (2.3). As previously mentioned, in applying the Shafranov formulae, the cylindrical values for both poloidal beta and inductance are used.

A comparison of Eq. (4.3) with the results obtained from the Baker-Mann code is shown in Fig. 4. Figure 4a shows the difference quantity $[\gamma(\text{Shafranov})-\gamma(\text{Code})/\gamma(\text{Code})]$ as a function of β_p. Figure 4b shows this difference as a function of aspect ratio. In both cases, the internal inductance parameter (ℓ_i) is held constant at 1.5. Both figures show good accuracy for the Shafranov formulae, except at low aspect ratios ($\lesssim 2$) and high poloidal betas ($\gtrsim 0.5$).

A comparison of Eq. (4.3) for different values of ℓ_i is shown in Fig. 5 for an aspect ratio of 3. The accuracy decreases as ℓ_i increases, which physically relates to a pinching of the plasma current column.

It is interesting to note that, if the toroidal values of ℓ_i and β_p in the Shafranov formulae are used, the results are less accurate than if the cylindrical values are employed (Fig. 6).

B. Magnetic Axis and Flux Surface Shift

To first order in ε, the equilibrium magnetic flux surfaces of a plasma enclosed within a perfectly conducting toroidal shell have nonconcentric circular cross sections. An analytic description of the center displacement (Δ_s) of the plasma surface at radius a', which defines the circular flux line enclosing the total plasma current, is given by Eq. (2.8). Figures 7 and 8 show a comparison of Δ_s with both the plasma center shift (Δ_c) and the magnetic axis shift (Δ_m) as calculated by the Baker-Mann code as a function of plasma profile and β_p.

Figure 7a shows the comparison for an aspect ratio of 3 and a diffuse plasma profile where the plasma surface lies close to the conducting boundary. As expected, the center shift of the plasma surface is small and differs substantially from the larger magnetic axis shift. The Shafranov formula (Δ_s) accurately predicts the code calculated shift (Δ_c) to within 13% for β_p values up to 0.5.

Figure 7c shows the comparison for a pinched plasma profile where the plasma surface is approximately at one-half the conducting boundary radius. For this case, the code calculated shift (Δ_c) is comparable to the magnetic axis shift. The error in the Shafranov formula (Δ_s) is apparent because it predicts a shift greater than Δ_m for β_p values less than 0.1. This result is clearly nonphysical and is due to a violation of the validity condition for Eq. (2.8), which requires $\Delta_s \ll a$. Figure 7b shows the comparison for the intermediate case where the plasma surface is approximately at three-quarters of the conducting boundary radius. Equation (2.8) remains accurate to within 15% for β_p values up to 0.5. For all cases illustrated in Figs. 7 through 9, the cylindrically defined internal inductance per unit length (ℓ_i) was held fixed at 1.5.

Figure 8 shows the comparison for an aspect ratio of 5.2, whereas Fig. 9 illustrates the dependence of Δ_c and Δ_m on aspect ratio β_p and plasma profile. Based on this study, the Shafranov shift formula [Eq. (2.8)] is generally valid for shifts less than one-tenth of the toroidal minor radius ($\Delta_s/a \lesssim 0.1$).

V. APPLICATIONS TO ZT-40M

The ZT-40M reversed field pinch uses an Inconel toroidal vacuum vessel with a major radius of 114 cm and minor radius of 19.7 cm, surrounded by a close-fitting conducting shell (Fig. 10). The poloidal field windings consist of 36 toroidally wound coils with approximately uniform azimuthal spacing. To initiate a plasma discharge, the shell incorporates an insulated gap positioned in a plane perpendicular to the toroidal direction. During the discharge, the plasma is held in equilibrium by image currents on the inside surface of the shell. For regions away from the gap, the image currents set up an interior equilibrium poloidal field distribution that is essentially unaffected by the external windings for time scales less than the shell poloidal field diffusion time ($\tau \approx 3$ ms for ZT-40M). However, at the minor gap, the internal-external field mismatch drives field perturbations that can distort the plasma's magnetic surfaces. It is, therefore, important to externally match the equilibrium field distribution in the vicinity of the gap during the entire discharge.

A. Design of the Poloidal Field Winding Distribution

Because the poloidal field windings on ZT-40M cannot be individually controlled, a given winding distribution can only provide a correct equilibrium field distribution for a specific set of values for plasma beta and internal inductance. Thus, for design purposes, it is necessary to estimate plasma beta and internal inductance for nominal machine operation.

Initially, this was accomplished by using the Shafranov formulae to determine the equilibrium poloidal field distribution for the expected range of operation ($0 \lesssim \beta_p \lesssim 0.2$, $1.0 \lesssim \ell_i \lesssim 1.8$). Fortuitously, this design criterion predicted a nearly uniform $B_p(a)$ distribution, since the Shafranov asymmetry factor (Λ) was close to zero. The analytic calculation was subsequently checked with the Baker-Mann Code for the field and pressure profiles described in the Appendix. Both approaches yielded similar results,

as shown in Fig. 11, which plots the equilibrium field ratio γ for ZT-40M [Eq. (4.3)] as a function of β_p and ℓ_i.

For times longer than the vertical field diffusion time of the shell, plasma equilibrium is strongly dependent on the external poloidal field distribution. The external windings must provide the full equilibrium vertical field necessary to balance the hoop stress of the discharge column. For $\varepsilon << 1$, the equilibrium vertical field is approximately given by[4]

$$|B_z| = \frac{\mu_o I_\phi}{4\pi R}\left[\ln\left(\frac{\rho R}{a'}\right) + \Lambda - \frac{1}{2}\right] , \tag{5.1}$$

where R and a' represent the major and minor radius of the discharge column, respectively. A plot of the poloidal winding vacuum field for ZT-40 under full 600-kA operation is illustrated in Figs. 12 through 14.* The vertical field magnitude agrees with Eq. (5.1) for the $\Lambda = 0$ design condition. However, to the extent that Λ deviates from zero during a discharge, an additional vertical field correction is necessary to minimize plasma drift.

B. Calculation of Internal Inductance

For predicting and interpreting some equilibrium aspects of an RFP, it is necessary to know the behavior of ℓ_i, the internal inductance, as a function of discharge conditions. In the absence of experimental magnetic field measurements, ℓ_i is computed from a model that describes the RFP equilibrium magnetic fields. A brief description of the methodology follows.

The RFP is characterized by a high shear magnetic field configuration where the toroidal field is reversed on the plasma exterior with respect to its value on axis. This field configuration is postulated to be a consequence of plasma relaxation by a process involving field line reconnection.[7] The relaxed states are independent of initial conditions and can be described by the dimensionless parameters F and Θ, where

*The asymmetric effects of the discrete iron cores are not explicitly included.

$$F = \text{Field Reversal Parameter} = \frac{B_\phi(a)}{\langle B_\phi \rangle} = \frac{B_\phi(a)}{(2/a^2)\int_0^a B_\phi(r)\, r\, dr} \quad , \tag{5.2}$$

$$\Theta = \text{Pinch Parameter} = \frac{B_p(a)}{\langle B_\phi \rangle} = \frac{B_p(a)}{(2/a^2)\int_0^a B_\phi(r)\, r\, dr} \quad , \tag{5.3}$$

and B_ϕ denotes the toroidal magnetic field.

For the force-free ($\beta = 0$) case, Taylor suggested the relaxed fields are eigenfunctions of the equation[7]

$$\nabla \times \vec{B} = \mu \vec{B} \quad , \tag{5.4}$$

where μ is a constant ($\mu = 2\Theta/a$). In cylindrical geometry, the solution of Eq. (5.4) yields the Bessel function field profiles

$$B_\phi(r) = B_t J_o(\mu r) \quad \text{and} \tag{5.5}$$

$$B_p(r) = B_t J_1(\mu r) \quad , \tag{5.6}$$

where B_t denotes the toroidal field on axis. In practice, a modification of Eq. (5.4) is necessary to accurately match the observed behavior of F and Θ in ZT-40M. Using the approximation that cross field current flow is small in low beta plasmas, the modified force-free equation is given by

$$\nabla \times \vec{B} = \mu(r)\vec{B} \quad , \tag{5.7}$$

where $\mu(r)$ is a spatially dependent parameter that specifies the plasma current profile. The functional dependence of $\mu(r)$ for a given pinch discharge is obtained by iterating Eq. (5.7) such that the calculated values of F [Eq. (5.2)] and Θ [Eq. (5.3)] agree with experimental measurements. The

Modified Bessel Function Model (MBFM),* in essence, modifies Taylor's relaxed field profiles to allow for zero plasma current density at the liner wall. A zero-dimensional plasma simulation code using the MBFM has successfully simulated the electrical and magnetic properties of RFP behavior.[8-11] Figure 15 shows a comparison between the Bessel Function Model (BFM) and MBFM field and current density profiles for the nominal ZT-40M operating condition of $\Theta = 1.6$.

Using the MBFM field profiles and Eq. (2.5), the nominal emu internal inductance per unit length (ℓ_i) of ZT-40M as a function of Θ can be approximated in the range ($0 < \Theta < 1.9$) by the polynomial

$$\ell_i(\Theta) = [0.5 + 0.113\Theta^2 - 0.194\Theta^3 + 0.556\Theta^4 - 0.198\Theta^5] \qquad (5.8)$$

and is illustrated in Fig. 16a. For comparison, $\ell_i(\Theta)$ for the BFM profiles is illustrated in Fig. 16b. It is important to note that relationship between ℓ_i and Θ is not unique but is rather dependent on the assumed field model.

The MBFM profiles, used to calculate $\ell_i(\Theta)$, are derived from a force-free ($\beta = 0$) model. Thus, in principle, the functional dependence of ℓ_i on Θ is not consistent for describing a finite β plasma. In practice, however, the correction to $\ell_i(\Theta)$ for poloidal betas less than 0.2 on ZT-40M are less than 20%. This correction results from the dependence of Θ on poloidal beta as shown in Fig. 17, which plots Θ vs β_p for fixed ℓ_i as calculated by the Baker-Mann code. For large aspect ratios (>5) and realistic RFP poloidal betas ($\lesssim 0.2$), the finite beta correction to $\ell_i(\theta)$ is comparable to errors resulting from uncertainties in field or pressure profiles in an ideal MHD derivation of internal inductance.

*The MBFM is not related to the mathematically defined Modified Bessel Functions.

C. The Use of External Field Measurements to Determine the Asymmetry Factor

Equation (4.3) can be solved to give the asymmetry factor Λ in terms of the field ratio γ and the inverse aspect ratio ε giving

$$\Lambda = \varepsilon(\gamma - 1)/(\gamma + 1) \quad . \tag{5.9}$$

Thus a two point measurement of the poloidal field gives the asymmetry factor.

Alternatively, Λ can be expressed in terms of the first two coefficients of a Fourier expression of the field. If one assumes symmetry about the midplane of the torus, the poloidal field at R = a can be expanded in a Fourier cosine series as follows.

$$B_p(\theta) = \frac{a_o}{2} + \sum_{n=1}^{\infty} a_n \mathrm{Cos}(n\theta) \quad , \tag{5.10}$$

with

$$a_n = \frac{1}{\pi} \int_o^{2\pi} B_p(\theta)\mathrm{Cos}(n\theta)d\theta \quad . \tag{5.11}$$

Keeping only the first two terms of Eq. (5.10) yields

$$B_p(\theta) \simeq \frac{a_o}{2} + a_1\mathrm{Cos}(\theta) = \frac{a_o}{2}\left[1 + \frac{2a_1}{a_o}\mathrm{Cos}\theta\right] \quad . \tag{5.12}$$

Comparing this expression with Eq. (2.1) for a = a´ gives

$$\Lambda = 2a_1/(a_o\varepsilon) \quad , \tag{5.13}$$

and $B_o(a) = a_o/2$ is the average poloidal field at the wall.

Further making use of Eqs. (2.3) and (5.10) yields

$$\Lambda \equiv \beta_p + \frac{\ell_i}{2} - 1 = 2\left(\frac{a}{R}\right) \frac{\int_o^{2\pi} B_p(\theta)\cos\theta d\theta}{\int_o^{2\pi} B_p(\theta) d\theta} \quad . \tag{5.14}$$

Thus to first order in ε, the asymmetry factor is obtainable in terms of the first two Fourier components of the poloidal field at the wall. These components are measured in ZT-40M with external pickup loops.* The field ratio γ is related to the Fourier components as follows.

$$\gamma = \left[1 + (2a_1/a)\right]/\left[1 - (2a_1/a)\right] \quad . \tag{5.15}$$

Note that only a linear combination of β_p and ℓ_i is obtainable from a measurement of Λ. Further assumptions or measurements are needed to obtain β_p or ℓ_i individually.

D. Sample β_p Estimate

If Eq. (5.8) is used to estimate ℓ_i from experimental measurements of Θ, we can use the external loop measurements of the Fourier components to get a corresponding estimate of β_p vs time. Sample plots of Λ and β_p for Shot No. 7106 (flat-top current operation) are shown in Fig. 18.

The Shafranov formulae are valid for a single perfectly conducting shell, and the presence of the resistive liner inside the aluminum shell in ZT-40M can affect the validity of this approach. The diffusion of the fields into the aluminum shell also affects the measured value of Λ. For example, if the current in and/or pressure at the liner is non-negligible, the results of both the Shafranov formulae and the computer calculations can be rendered invalid for the actual experiment. Similarly, appreciable non-axisymmetric perturbations in the discharge from field errors, for example, can also invalidate this approach.

*Courtesy of C. J. Buchenauer.

VI. CONCLUSIONS

The Shafranov analytic formulae for equilibrium poloidal field distributions give accurate results (within 5%) for aspect ratios above 2.0, poloidal betas below 50%, and for current channels exceeding one-third the minor radius of the conducting boundary. The analytic description for the center displacement of the plasma surface is accurate (within 15%) for aspect ratios above 2 and poloidal betas below 50%, provided the center shift is less than one-tenth of the minor boundary radius. The Shafranov formulae provide a convenient method for utilizing external field measurements to determine the equilibrium behavior of an axisymmetric toroidal RFP discharge over a wide range of plasma conditions.

ACKNOWLEDGMENTS

The authors thank the following persons: R. A. Gribble for contributions in the area of the field modeling of ZT-40M, S. Hue for assistance in updating and making additions to the equilibrium code, and A. Haberstich and C. J. Buchenauer for the ZT-40M external field measurements.

REFERENCES

1. V. D. Shafranov, "Plasma Equilibrium in a Magnetic Field," in Reviews of Plasma Physics V2, edited by M. A. Leontovich (Consultants Bureau, New York, 1966), p. 103-151.

2. V. S. Mukhovatov and V. D. Shafranov, "Plasma Equilibrium in a Tokamak," Nucl. Fusion 11, 605 (1971).

3. D. A. Baker and J. E. Hammel, "Experimental Studies of the Penetration of a Plasma Stream into a Transverse Magnetic Field," Phys. Fluids 8, 713 (1965).

4. D. A. Baker and L. W. Mann, "MHD Stability Studies of Numerically Obtained Toroidal Equilibria," Proc. 2nd Topical Conference on Pulsed High Beta Plasmas, Garching, Germany FR, 1972, IPP-1/127, pp. 69.

5. L. W. Mann and D. A. Baker, "Belt Pinch Equilibria Studies," Bull. Am. Phys. Soc. 18, 1327 (1973).

6. L. W. Mann and P. C. T. Van Der Laan, "Tokamak-Like Equilibria at Beta Close to Unity," Nucl. Fusion 19, 1029 (1979).

7. J. B. Taylor, "Relaxation of Toroidal Plasma and Generation of Reverse Magnetic Fields," Phys. Rev. Lett. 33, 1139 (1974).

8. J. W. Johnston, "A Plasma Model for Reversed Field Pinch Circuit Design," Plasma Phys. 23, 187 (1981).

9. R. F. Gribble and K. F. Schoenberg, "Plasma Resistance Determination in a Reversed Field Pinch from External Discharge Characteristics," Bull. Am. Phys. Soc. 25, 1026 (1980).

10. K. F. Schoenberg and R. F. Gribble, "Plasma Resistance, Conductivity Temperature and Flux Consumption Measurements on ZT-40M," Bull. Am. Phys. Soc. 26, 1041 (1981).

11. K. F. Schoenberg, R. F. Gribble, and J. A. Phillips, "Zero-Dimensional Simulations of Reversed Field Pinch Experiments," LA-UR-82-778 (1982), submitted to Nucl. Fusion.

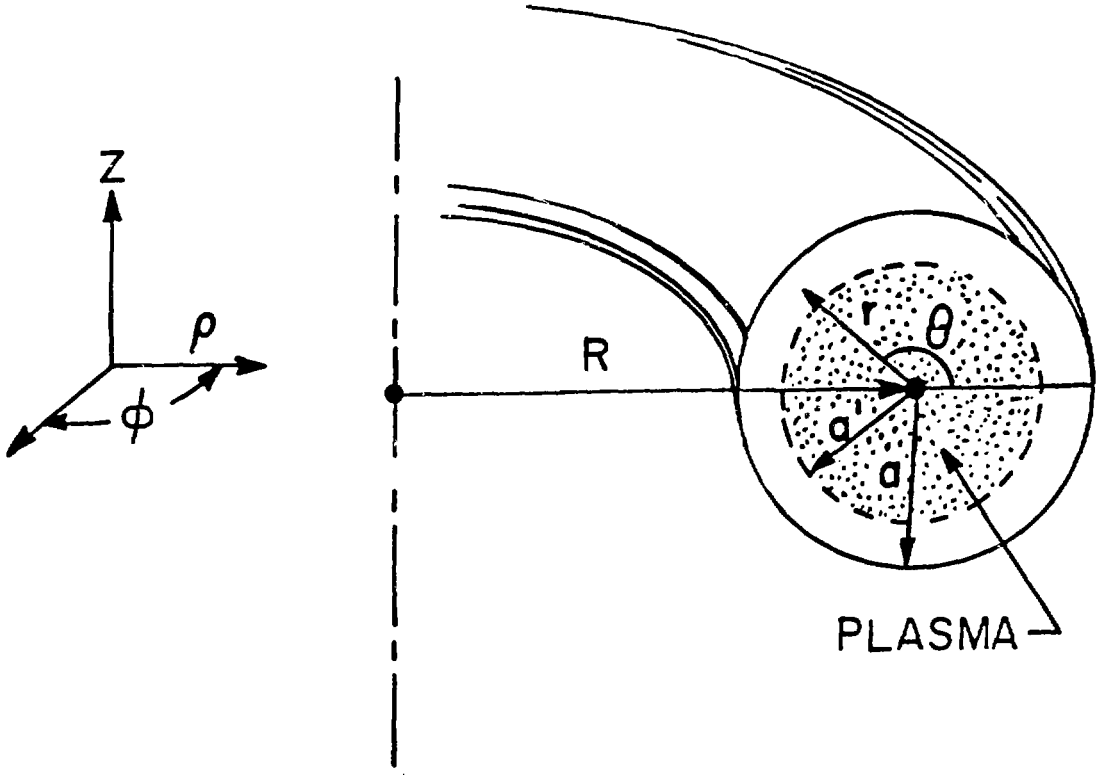

Fig. 1.
The spatial coordinate systems employed in the analytic and numerical poloidal field equilibrium calculations.

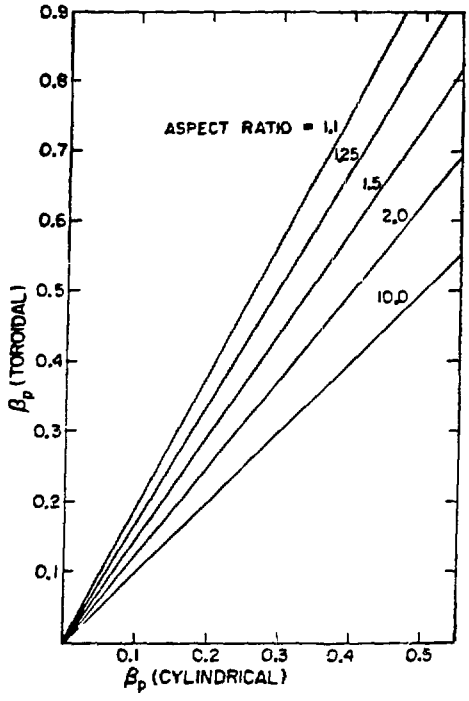

Fig. 2.
β_p for a torus vs β_p for a cylinder as a function aspect ratio.

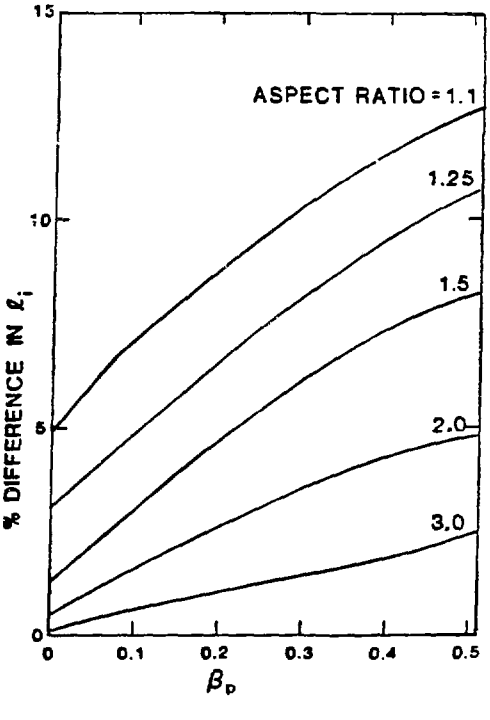

Fig. 3.
Percentage of difference in ℓ_i for a torus with respect to ℓ_i for a cylinder as a function of β_p for various aspect ratios.

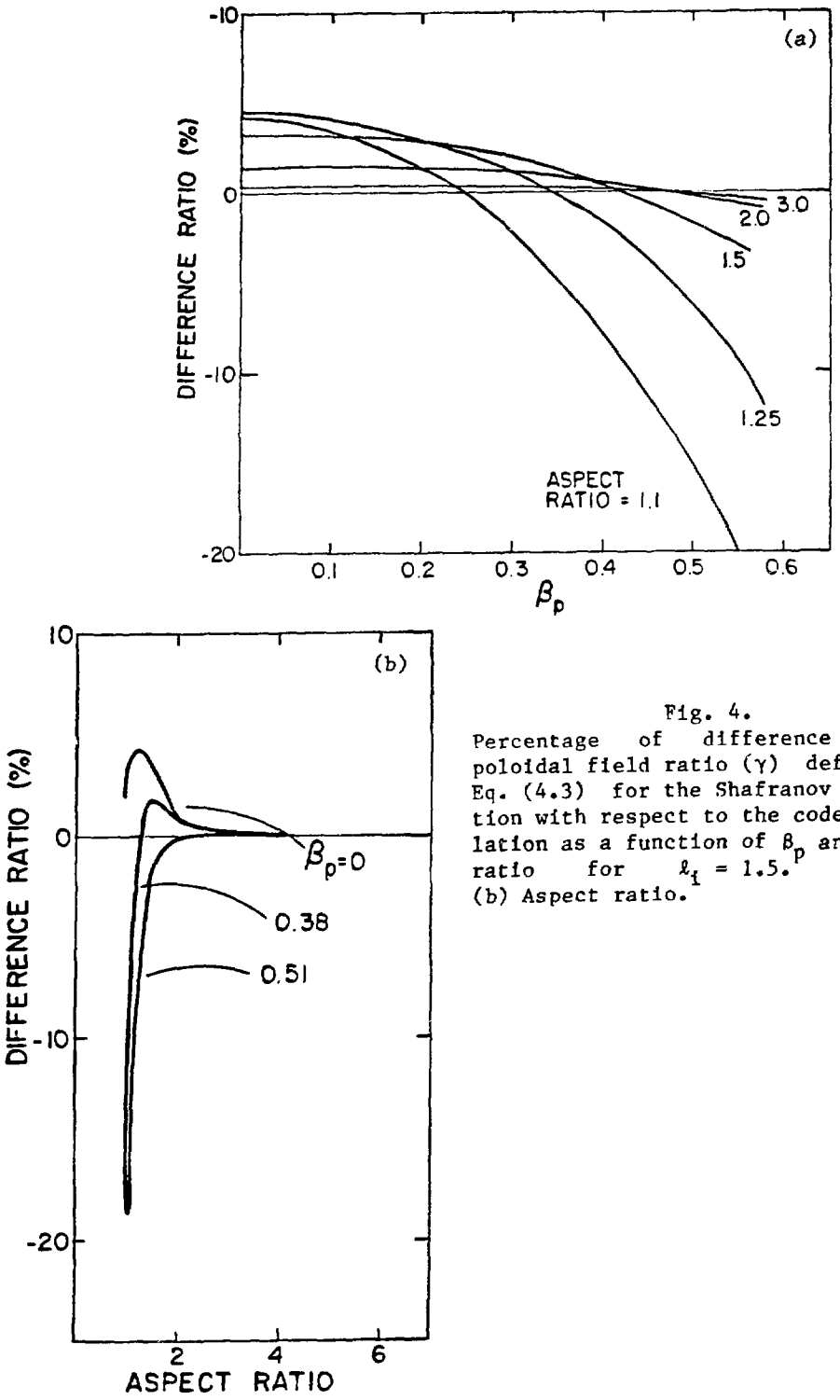

Fig. 4.
Percentage of difference in the poloidal field ratio (γ) defined by Eq. (4.3) for the Shafranov calculation with respect to the code calculation as a function of β_p and aspect ratio for $\ell_i = 1.5$. (a) β_p; (b) Aspect ratio.

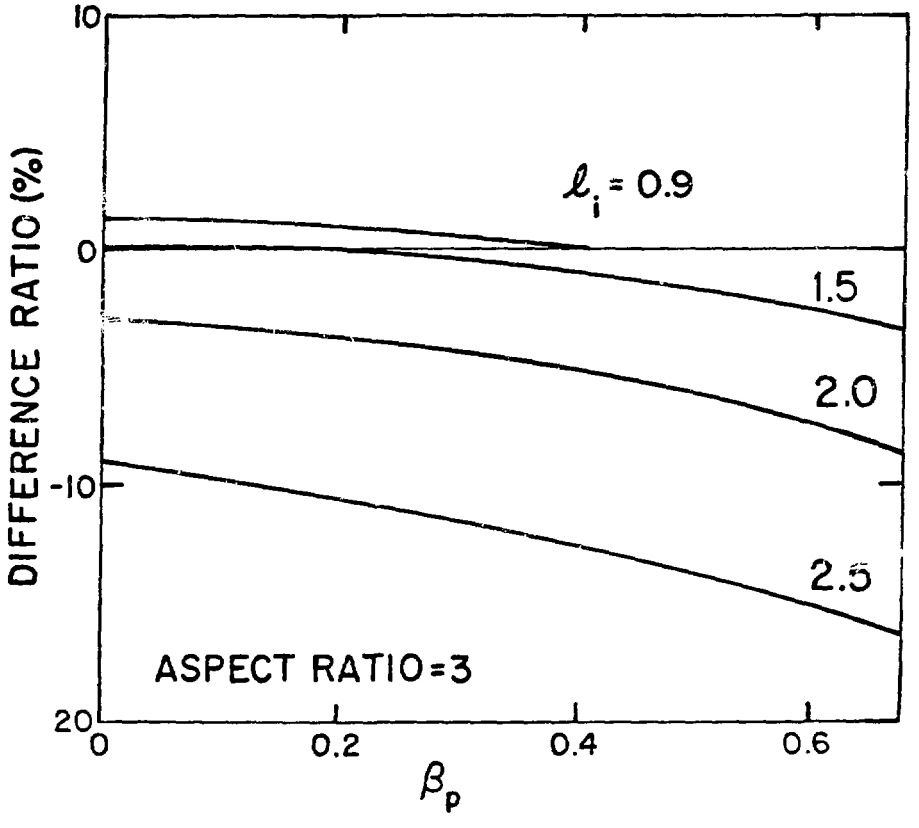

Fig. 5.
Percentage of difference in γ as a function of β_p and ℓ_i for an aspect ratio of 3.

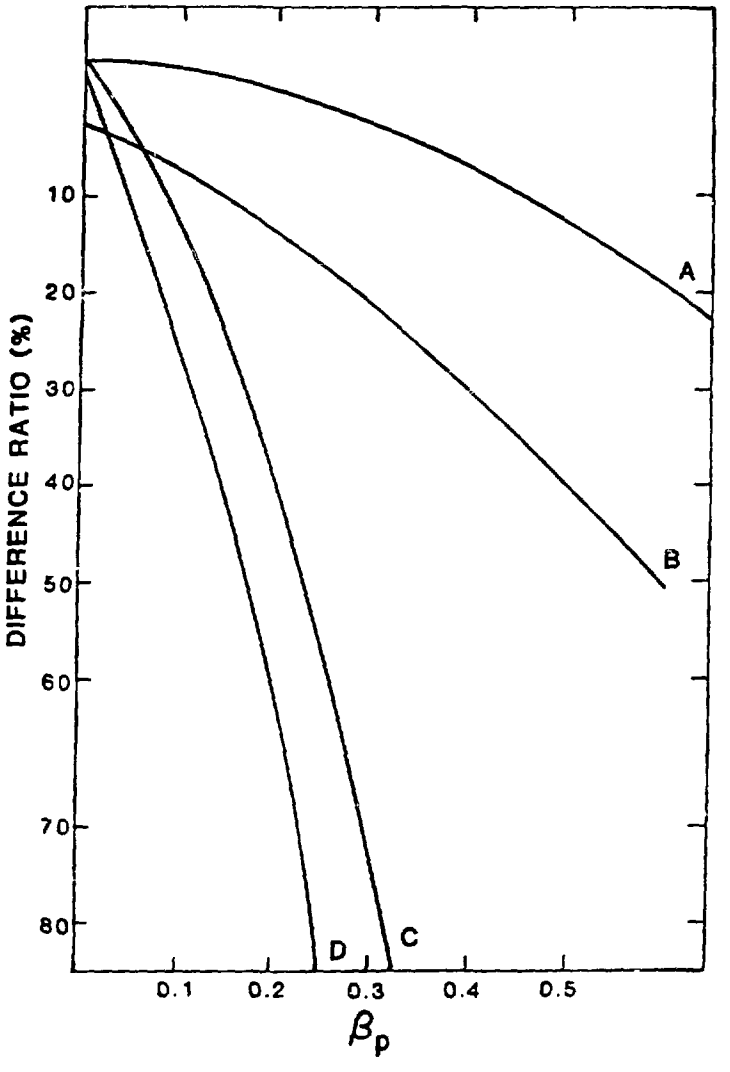

Fig. 6.

Percentage of difference in γ as a function of β_p for $\ell_i = 1.5$ and an aspect ratio of 3, where β_p and ℓ_i are defined as follows. (A) β_p (cylindrical), ℓ_i (cylindrical); (B) β_p (cylindrical), ℓ_i (toroidal); (C) β_p (toroidal), ℓ_i (cylindrical); (D) β_p (toroidal), ℓ_i (toroidal).

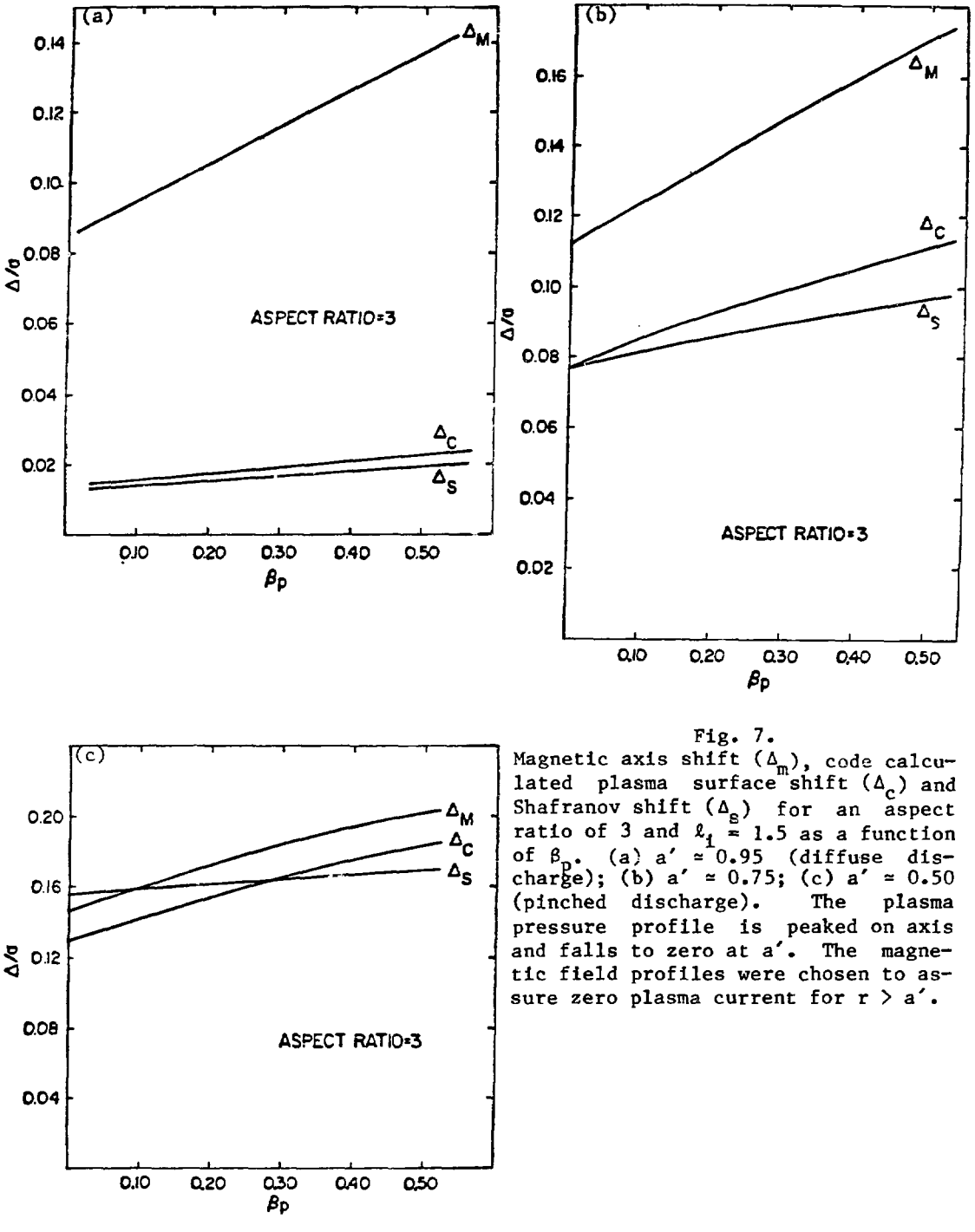

Fig. 7.
Magnetic axis shift (Δ_m), code calculated plasma surface shift (Δ_c) and Shafranov shift (Δ_s) for an aspect ratio of 3 and $\ell_i \approx 1.5$ as a function of β_p. (a) $a' \approx 0.95$ (diffuse discharge); (b) $a' \approx 0.75$; (c) $a' \approx 0.50$ (pinched discharge). The plasma pressure profile is peaked on axis and falls to zero at a'. The magnetic field profiles were chosen to assure zero plasma current for $r > a'$.

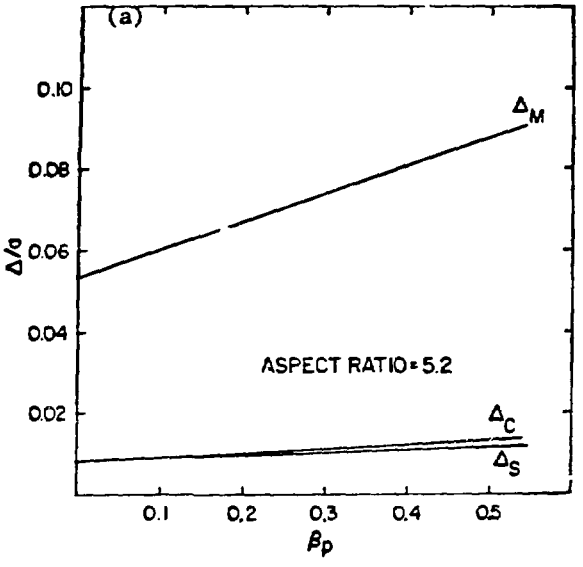

Fig. 8.
Shifts for an aspect ratio of 5.2 and $\ell_i = 1.5$ as a function of β_p. (a) $a' \approx 0.95$; (b) $a' \approx 0.50$.

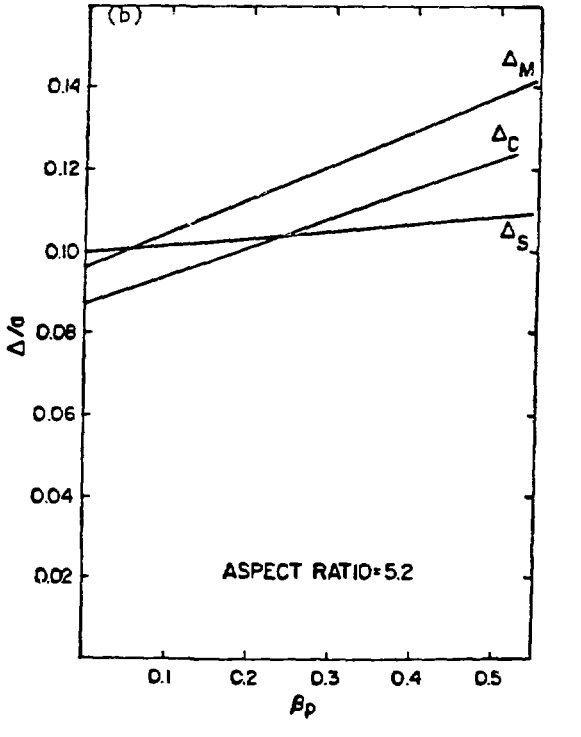

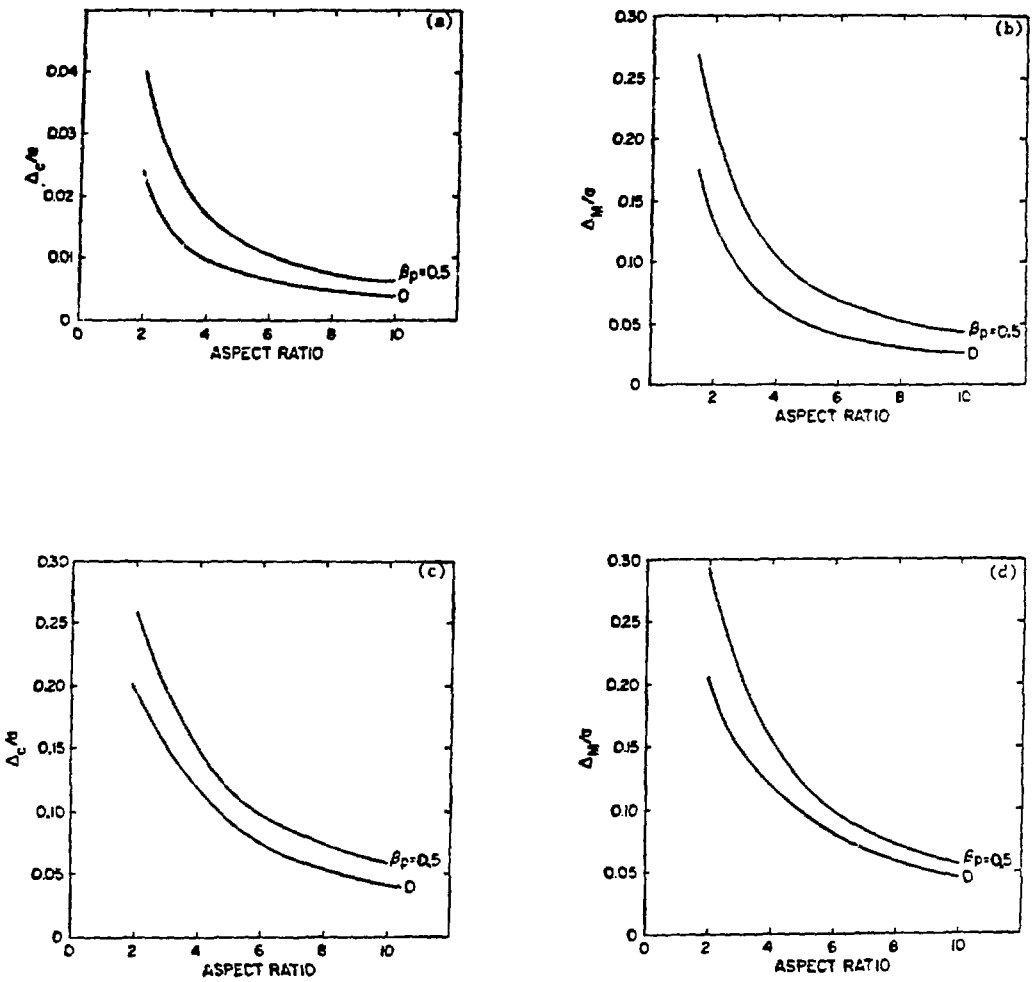

Fig. 9.
Magnetic axis shift (Δ_m) and plasma surface shift (Δ_c) as a function of β_p and aspect ratio for ℓ_i = 1.5. (a) Δ_c for a diffuse discharge (a′ = 0.95); (b) Δ_m for a diffuse discharge (a′ = 0.95); (c) Δ_c for a pinched discharge (a′ = 0.5); (d) Δ_m for a pinched discharge (a′ = 0.5).

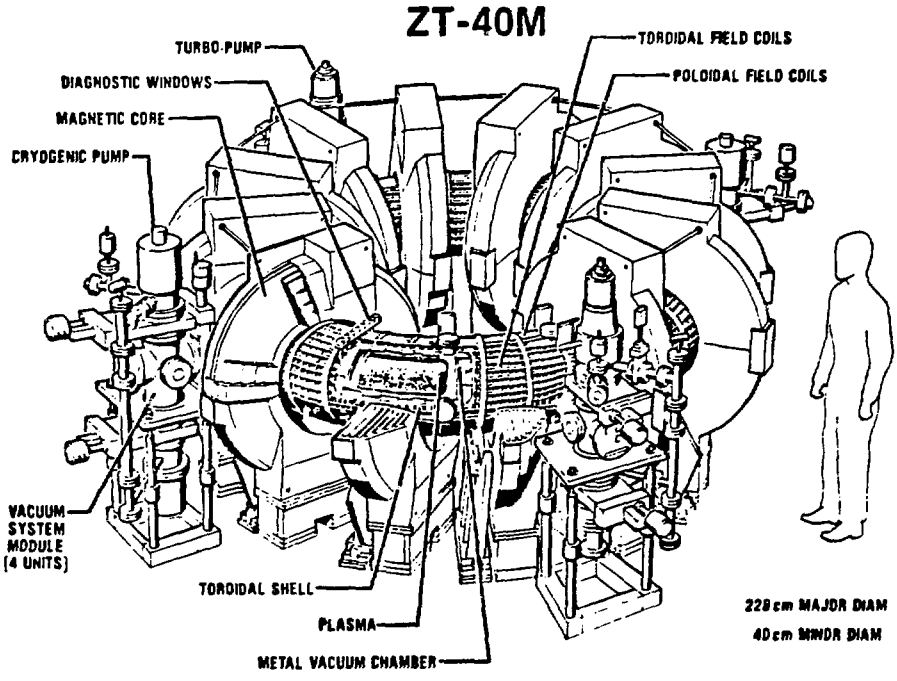

Fig. 10.
The ZT-40M experiment.

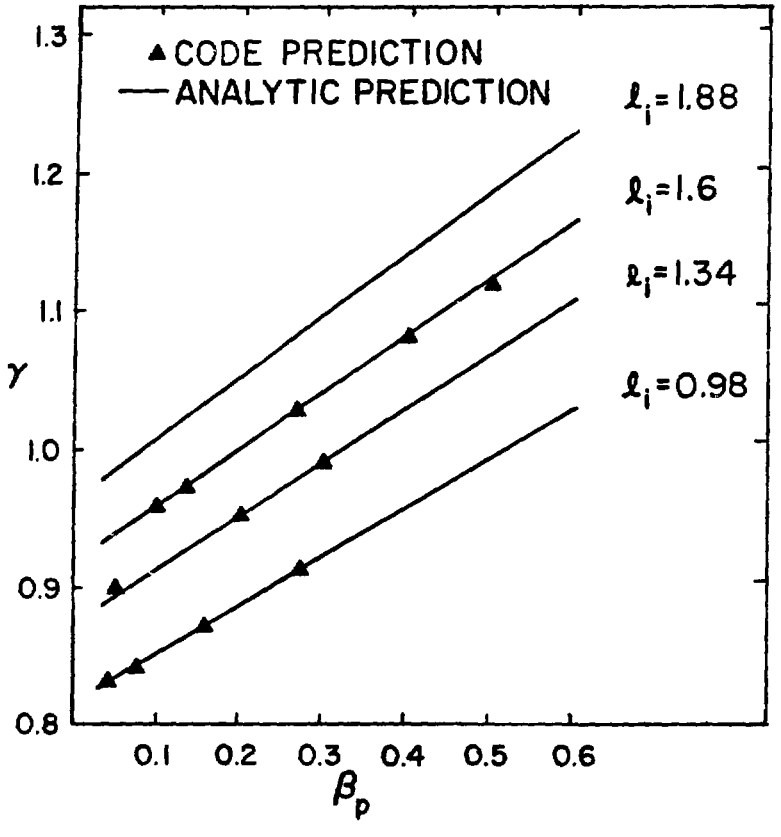

Fig. 11.
Analytic and numerical predictions for the poloidal field ratio defined by Eq. (4.1) on ZT-40M.

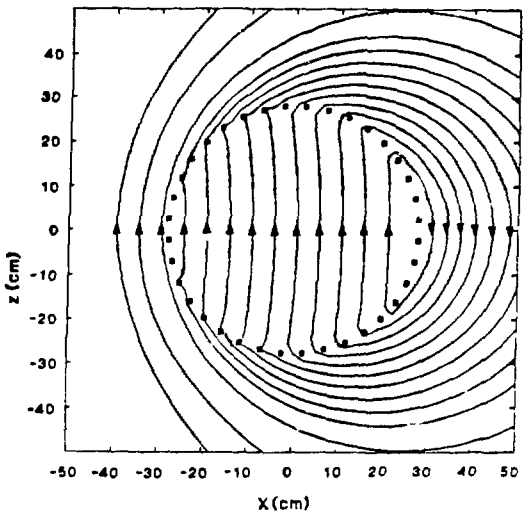

Fig. 12.
Vacuum poloidal field flux plot for ZT-40M under 600-kA operation.

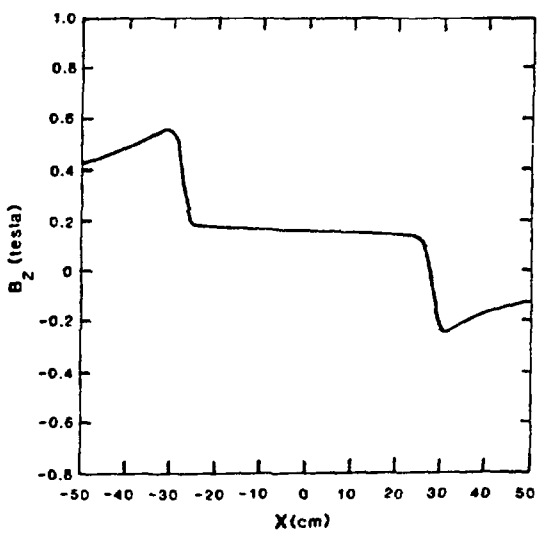

Fig. 13.
Vacuum vertical field magnitude for 600-kA operation.

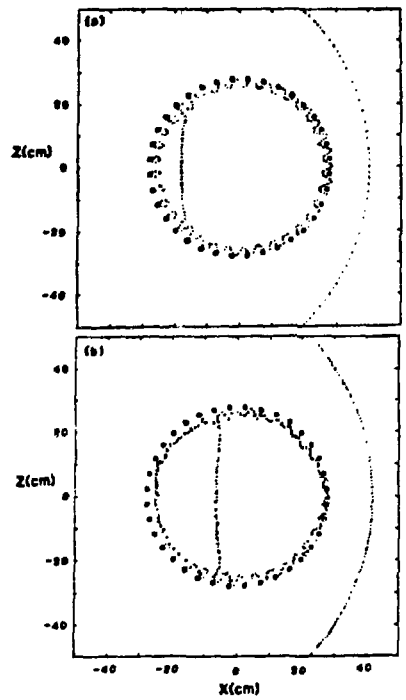

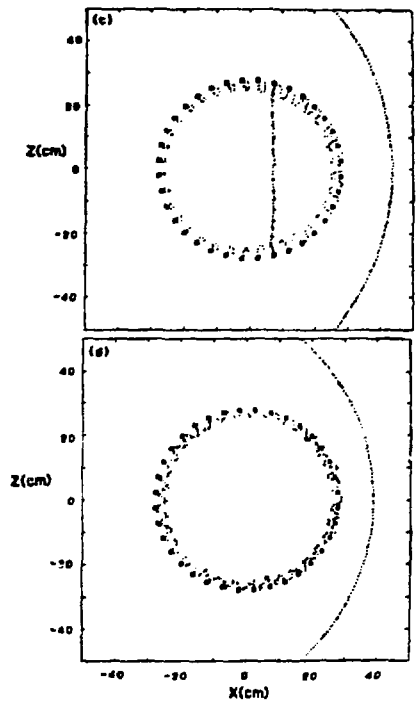

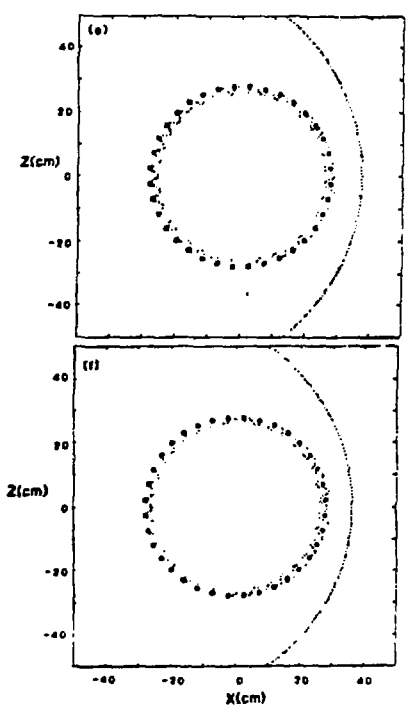

Fig. 14.
Vacuum poloidal field |B| contour plot for ZT-40M under 600-kA operation. (a) 0.15 T; (b) 0.16 T; (c) 0.17 T; (d) 0.18 T; (e) 0.19 T; (f) 0.20 T.

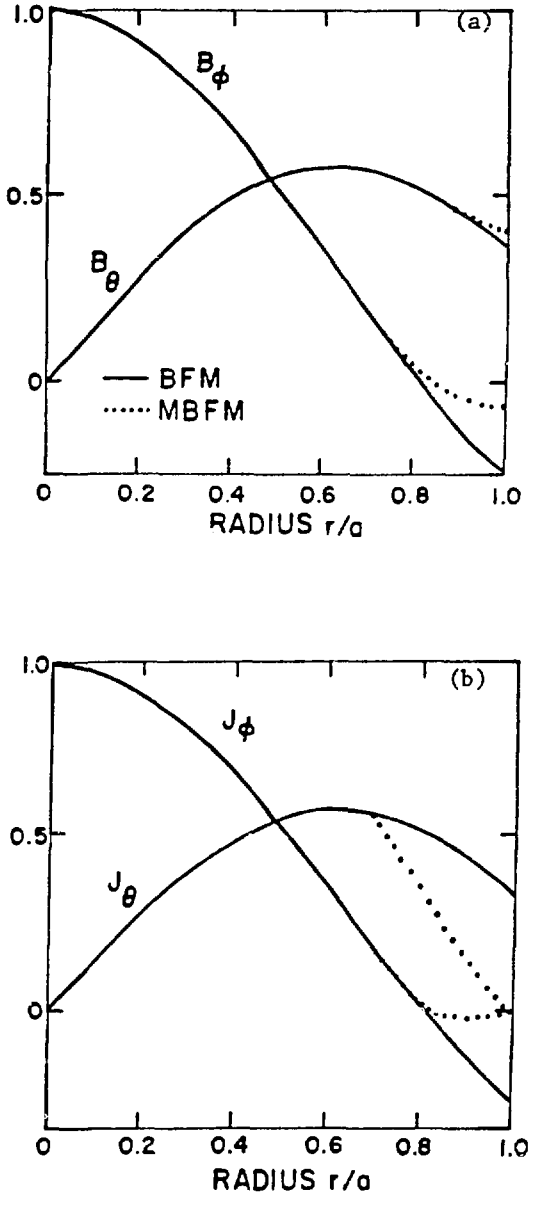

Fig. 15.
Toroidal and poloidal spatial profiles from the BFM and MBFM for (a) magnetic field and (b) current density.

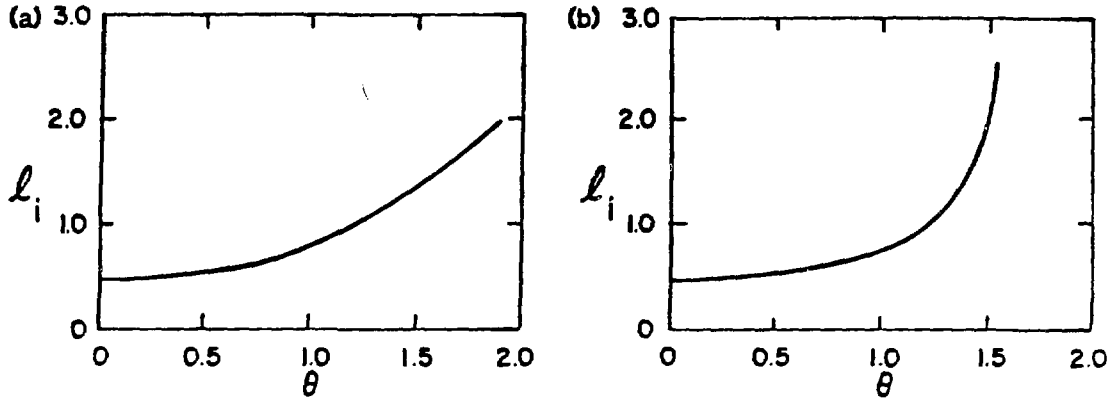

Fig. 16.
ZT-40M internal inductance per unit length (ℓ_i) as a function of the pinch parameter Θ for various field profiles. (a) MBFM; (b) BFM.

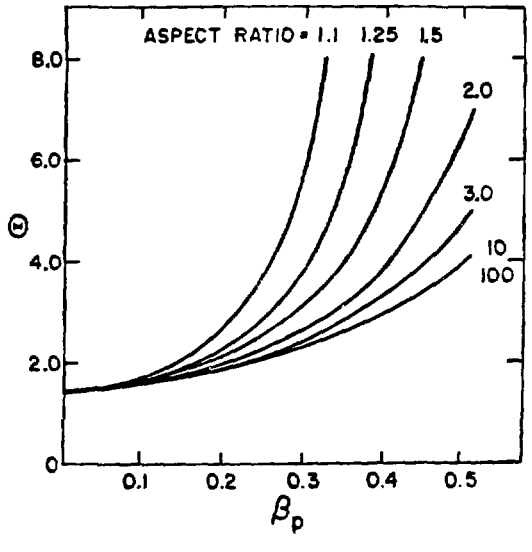

Fig. 17.
The variation of Θ with poloidal beta as a function of aspect ratio.

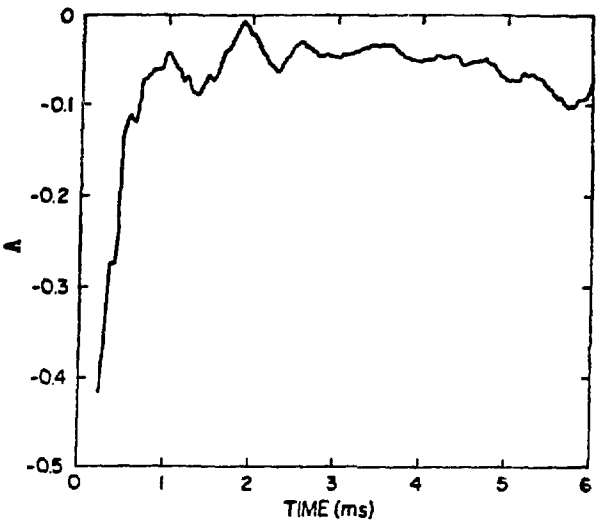

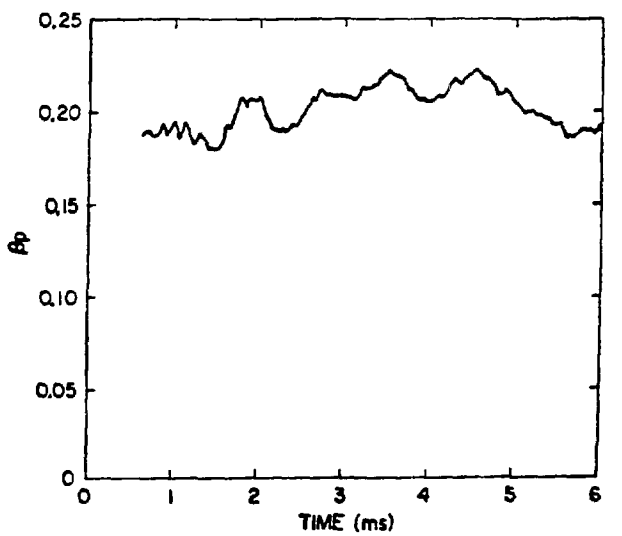

Fig. 18.
The measured time history of Λ and the estimated time history of β_p for a 190-kA ZT-40M discharge.

APPENDIX

CHOICE OF $p(\psi)$ AND $f(\psi)$ -- FUNCTIONS USED IN THE NUMERICAL ANALYSIS

The choice of source functions, used to obtain the curves given in this report, came from a subroutine that has proved very versatile for numerous RFP applications. For completeness we document the scheme here.

It is convenient for the user to input the source functions in terms of $p(r)$, $B_z(r)$, and $B_\theta(r)$ for a straight cylindrical model, rather than try to input directly the more abstract $p(\psi)$ and $f(\psi)$ functions. Any pair of the set $p(r)$, $B_z(r)$, or $B_\theta(r)$ is sufficient, since the third is obtainable from the pressure balance equation $\nabla p - \vec{J} \times \vec{B} = 0$ which, for a cylinder with no θ and z dependence, is

$$dp/dr + (B_\theta/r)d(rB_\theta)/dr + B_z dB_z/dr = 0 \quad . \tag{A-1}$$

This scheme has been implemented for two cases, where $p(r)$ and $B_z(r)$ are supplied in tabular form that the code fits with cubic splines and $p(r)$ and $B_\theta(r)$ are given as specific functions. The second case, used exclusively in this report, is detailed below.

The pressure is defined in three radial intervals as follows.

$$p(r) = a_1 r^3 + a_2 r^2 + a_3 r + a_4 \qquad 0 \leq r \leq r_m \quad , \tag{A-2}$$

$$p(r) = b_1 r^3 + b_2 r^2 + b_3 r + b_4 \qquad r_m \leq r \leq r_{c1}, \text{ and} \tag{A-3}$$

$$p(r) = 0 \qquad r_{c1} \leq r \leq r_w \quad . \tag{A-4}$$

The coefficients are determined so that $p(0) = p_o$, $p(r_m) = p_m$, and $p(r_{c1}) = 0$, with zero slopes at $r = 0$, r_m and r_{c1} (see Fig. A-1). The choice of two piece cubics, for an appropriate choice of the input parameters r_m, r_{c1}, p_o, and p_m, allows the pressure profile to be hollow or peaked on axis and to have a zero pressure annulus for $r > r_{c1}$.

The $B_\theta(r)$ field is defined over two intervals as

$$B_\theta^{(1)}(r) = 2B_{\theta max}\left(\frac{1}{A} - \frac{1}{r_{c2}}\right)r/\left[(r/A)^2 - 2r/r_{c2} + 1\right] \qquad 0 < r < r_{c2} \quad , \text{(A-5)}$$

$$B_\theta^{(2)}(r) = B_\theta^{(1)}(r_{c2})(r_{c2}/r) \qquad r_{c2} < r < r_w \quad . \text{(A-6)}$$

This choice of B_θ gives a diffuse field that approaches a linear radial dependence near the origin, peaks at $r = A$, and connects with a continuous first derivative at $r = r_{c2}$ to a $1/r$ B_θ field. To obtain a vacuum annulus $r_c < r < r_w$ with zero current density, set $r_{c1} = r_{c2} = r_c$. The code integrates Eq. (A-1), using the above expressions for p and B_θ, to determine $B_z(r)$. The flux function, defined as $\psi(r) = \rho_m \int_{r_w}^{r} B_\theta dr$, is then computed on a radial grid (ρ_m is the mean major radius for the toroidal problem). The inverse function $r = r(\psi)$ is then obtained from a spline interpolation from the grid. The final source functions are defined as

$$p(\psi) = p\big(r(\psi)\big) \quad \text{and} \qquad \text{(A-7)}$$

$$f(\psi) = \rho_m B_z\big(r(\psi)\big)/\mu_o \quad . \qquad \text{(A-8)}$$

The source functions are input to the code by way of the Grad-Shafranov equation (3.4) and solved by over-relaxation to give a toroidal solution corresponding to the cylindrical input model. The $\psi(r)$ function is used as a starting guess and loaded on the mesh before the iterations begin. There is one further subtlety that appears in this scheme; namely, the range of the ψ function $(0, \psi_{max})$ over the solution mesh changes during the over-relaxation iterations. Since the full range of the initial p(r) and $B_\theta(r)$ functions are desired, the value of ψ inputed to the arguments of $r(\psi)$ in Eqs. (A-7) and (A-8) is renormalized during the iterative process by multiplying ψ by the factor ψ_o/ψ_{max}. The maximum value ψ_{max} is updated after each complete iteration of the mesh. The quantity ψ_o is the initial ψ_{max} before the iterations begin.

Noting Fig. A-1, A is the minor radius to the peak of $B_\theta(r)$ in the straight cylindrical model used to generate the $p(\psi)$ and $f(\psi)$ functions. For the resulting toroidal solution, the equilibrium shift distorts the flux surfaces from circles, and A is a measure of the width of the current profile since it is approximately the mean radius from the magnetic axis to the peak poloidal field. For the calculations in this report, r_m was set to zero, giving broad pressure profiles peaked on axis; and in all cases, r_{c1} was set equal to r_{c2} (Fig. A-2).

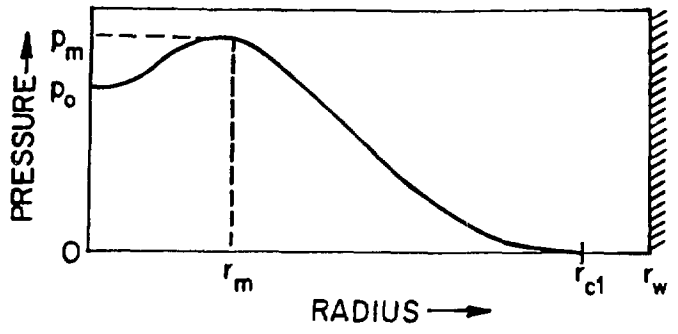

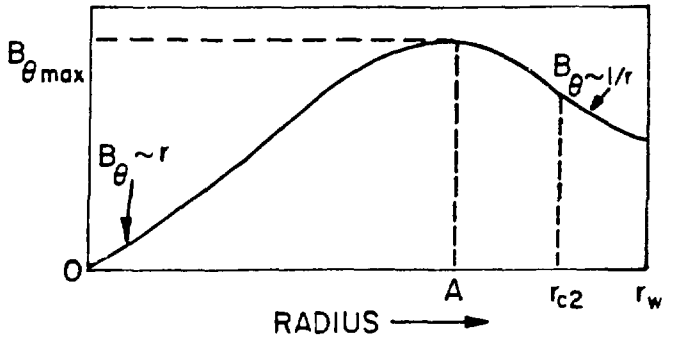

Fig. A-1.
A general schematic of the pressure and poloidal magnetic field profiles used in the numerical analysis.

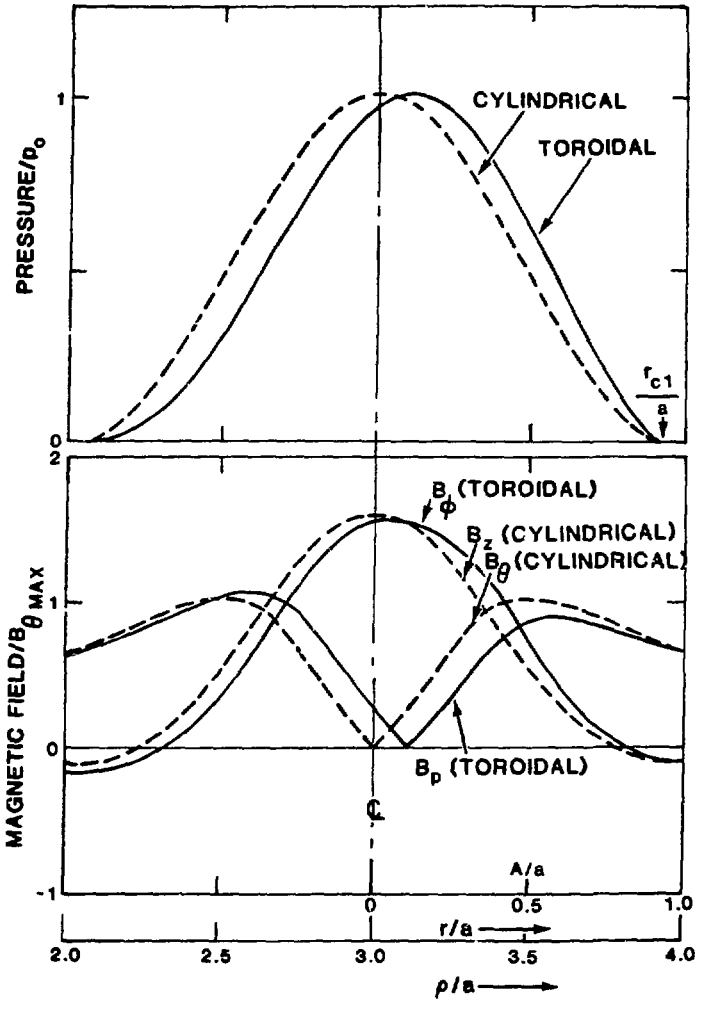

Fig. A-2.
Sample plots of the cylindrical input pressure and field profiles and the corresponding plots along the toroidal midplane obtained from the equlibrium code for the same value of peak pressure, p_o.